

Inverse Scattering Using a Joint $L1$ – $L2$ Norm-Based Regularization

Pratik Shah, *Student Member, IEEE*, Uday K. Khankhoje, *Member, IEEE*, and Mahta Moghaddam, *Fellow, IEEE*

Abstract—Inverse scattering problems suffer from ill-posedness and ill-conditioning, necessitating the use of regularization methods to get meaningful solutions. Commonly used regularizations are $L2$ norm based, but these generate over-smooth solutions. We propose a regularization method using both the $L1$ and $L2$ norms to obtain sharp object boundaries, while also achieving good interior reconstruction of the object permittivity. Knowledge about the permittivity can also be used as a priori information. The applicability of the method is demonstrated on synthetically generated data for two-dimensional (2-D) microwave imaging using the Born-iterative method (BIM). The optimization routine systematically estimates all parameters, while minimizing the cost function. Different objects chosen to represent realistic features have been considered to evaluate the performance. The reconstructed images indicate that the method can produce accurate object localization, shape identification, and good permittivity estimation.

Index Terms—Born-iterative method (BIM), compressive sensing, electromagnetic tomography, inverse problems, inverse scattering, microwave imaging, regularization.

I. INTRODUCTION

AN INVERSE scattering problem estimates the distribution of key physical parameters based on the measured samples of the scattered field. An electromagnetic inverse problem typically estimates permittivity and conductivity, whereas an acoustic inverse problem estimates, e.g., compressibility and density. Medical imaging, diffraction tomography, buried object detection, nondestructive testing, and industrial imaging are few examples where an inverse problem needs to be solved [1]. The electromagnetic inverse problem is usually formulated using the volume integral equation. The equation is nonlinear in general, since the electric field is a function of medium's properties and the internal fields of the object appear in the integral. A common practice is to use local optimization strategies and linearize the problem iteratively, solving for the parameters and the field at each iteration [2], [3]. Global optimization methods have also been considered but are generally less popular due to large computational costs [4].

Manuscript received May 05, 2015; revised December 04, 2015; accepted January 31, 2016. Date of publication February 12, 2016; date of current version April 05, 2016. The work of U.K. Khankhoje was supported by the INSPIRE Faculty Award (IFA-13 ENG-60) from the Department of Science and Technology, Government of India.

P. Shah and M. Moghaddam are with the Department of Electrical Engineering, University of Southern California, Los Angeles, CA 90089-1112 USA (e-mail: pratiks@usc.edu; mahta@usc.edu).

U. K. Khankhoje is with the Department of Electrical Engineering, Indian Institute of Technology Delhi, New Delhi 110016, India (e-mail: uday@alumni.caltech.edu).

Color versions of one or more of the figures in this paper are available online at <http://ieeexplore.ieee.org>.

Digital Object Identifier 10.1109/TAP.2016.2529641

In local optimization methods, a linear approximation of the inverse problem can be described by an unconstrained optimization problem with the objective: $\min_x \|y - Ax\|$, where y denotes measurements of the scattered field, A is the system matrix (which is a function of the internal fields), and x denotes the unknown parameter of interest, such as the dielectric contrast. Generally, the system is underdetermined as there are fewer measurements than the number of unknowns. In addition, the linear problem is ill-posed and ill-conditioned. To obtain a meaningful solution out of a multiplicity of solutions, various regularization schemes have used; generally inserted as a constraint or as a priori information. Regularization restricts the search space and thus reduces the degree of freedom in the solution. It also lessens the effect of noise, which is particularly important since the matrix A is usually ill-conditioned. $L2$ norm-based regularizations are commonly used ([5]–[8], among many), the Tikhonov method, L curve, and singular value decomposition (SVD) being examples of such methods [9], [10]. This type of regularization is known to produce an oversmooth solution [5], blur the edges/boundaries of the objects, overestimate the size of the object [11], and rescale the solution [12].

Since the recent advent of compressive sensing [13], $L1$ norm-based methods have gained popularity, showing promising results when the signal (x , in our case) is sparse in some basis, or is compressible [14], [15] and the system matrix obeys the restricted isometric property (RIP). In such cases, the solution has sharp edges and preserves discontinuities [11]. Work on compressive sensing in inverse scattering problems started with point-like targets [16]–[21], and moved on to small-size objects of smaller size [22]–[25]. In the latter, the inverse scattering problem was formulated as a Bayesian compressive sensing problem, and was shown to work without the need to satisfying RIP. However, their approach did not consider complex-valued matrices, thus obstructing the use of the colocations sparsity of real and imaginary values of the unknown vector. Other studies on compressive sensing in inverse scattering include total variation (TV)-based approach and sparsifying the domain using a wavelet transform [26]. The TV-based approach requires RIP to hold in order to get exact recovery [27], which does not necessarily hold true usually [28]. A recent article [29] based on this approach recovers the dielectric contrast within the Born approximation, although if the object has a smoothly varying profile of contrast, the assumption on sparsity fails.

In this paper, an innovative joint norm-based approach—based on the use of $L1$ and $L2$ norms as regularization—is proposed and is applied to a two-dimensional (2-D) microwave tomographic imaging problem. We utilize the Born-iterative

method (BIM) to recover contrasts higher than those allowed under the Born approximation. The joint norm-based approach can satisfy the RIP, if the L_2 regularization parameter is set correctly. The proposed method estimates the regularization parameters and updates them as and when required. The approach exhibits the features of both norms—sharp at edges and smooth everywhere else.

The main contributions of this work are as follows: 1) the derivation of a joint norm-based inverse scattering strategy that, unlike similar state-of-art methods [23]–[25], [29], effectively handles complex valued matrices and vectors for contrasts higher than the Born approximation and objects larger than point-like objects; 2) the introduction of an L_2 norm regularizer in the compressive sensing framework in order for electromagnetic imaging problems to satisfy RIP; and 3) an extension to the spectral gradient method by applying bound constraints and incorporating L_2 norm regularization.

This paper is organized as follows. In Section II, the problem formulation is detailed and discussed in two sections. Section III discusses the applicability of compressive sensing for inverse scattering problems and Section IV describes the joint norm formulation and outlines the inversion algorithm. Evaluation of the algorithm on simulated data is performed in Section V. Finally, conclusion and future directions are drawn in Section VI.

II. BASIC THEORY AND INVERSE PROBLEM FORMULATION

A. Inverse Scattering Problem

The scattering problem is governed by the following scalar electric field volume integral equation, expressed for a heterogeneous, isotropic, nonmagnetic medium in a region D , with measurement points on a surface S that encloses D , as [30]

$$E_s(r) = k_b^2 \int_D G(r, r') \chi(r') E(r') dv', \quad r \in S, r' \in D \quad (1)$$

where $E_s(r) = E(r) - E_i(r)$ is the scattered electric field in terms of the total field $E(r)$ and the incident field $E_i(r)$, $G(r, r')$ is the Green's function, k_b is the wavenumber of the background medium with lossless permittivity, ϵ_b is the lossless relative permittivity of a background medium, and $\chi(r) = [\epsilon_r(r')/\epsilon_b - 1] - j[(\sigma(r') - \sigma_b)/(\epsilon_b \epsilon_0 \omega)]$ is the dielectric contrast in terms of the permittivity and conductivity contrast, where the subscript r denotes the relative permittivity and σ_b is the background conductivity. In what follows, we assume a z -independent 2-D scatterer and the electric field to be polarized along the z -direction, corresponding to a transverse magnetic (TM) polarization.

The inverse problem deals with determining the dielectric contrast, $\chi(r)$, $r \in D$, of an unknown medium, given some observations of the scattered field, $E_s(r)$, $r \in S$. Due to the presence of the electric field under the integral sign, (1) is nonlinear, which can be linearized by using an estimate of the electric field. This leads to a matrix equation of the form $y = Ax$ that can be solved in an iterative manner; the BIM [31] is one such method. Here, $y \in \mathbb{C}^m$ contains m measurements of the scattered field, $x \in \mathbb{C}^n$ is the dielectric contrast

for a domain discretized into n unknown values of contrast (in the pixel basis), and each element of $A \in \mathbb{C}^{m \times n}$ contains the product of the Green's function of the background and the estimated field. The linearized inverse problem is still ill-posed and ill-conditioned, and requires regularization for successful solution.

B. Forward Problem

At every iteration of the BIM, we compute the electric field based on the current estimate of the dielectric contrast. For solving the forward electromagnetic scattering problem, we use a 2-D vector element-based finite-element method (FEM) [32]. In this implementation of the FEM, we employ first-order Whitney edge elements as basis functions for the total electric field, and a first-order absorbing boundary condition to terminate the computational domain. This results in a sparse set of equations that is solved very efficiently using a direct solver.

III. APPLICABILITY OF COMPRESSIVE SENSING

In the compressive sensing framework, an accurate reconstruction of a sparse signal x can be obtained in the following reconstruction problem:

$$\min \|x\|_1 \quad \text{s.t.} \quad \|Ax - y\| \leq \epsilon_n \quad (2)$$

if the RIP holds, where ϵ_n bounds the amount of the noise in the data. The RIP is defined as [27]: given a matrix A and $\delta_s \in (0, 1)$, if the following relation holds:

$$(1 - \delta_s) \|x_s\|_2^2 \leq \|Ax_s\|_2^2 \leq (1 + \delta_s) \|x_s\|_2^2 \quad (3)$$

for all s -sparse vectors x_s , A is said to obey the RIP to order s with a restricted isometry constant δ_s .

To validate the RIP for the inverse scattering problem in more rigorous way, we use the properties of the matrix norm. Rearranging the terms in (3), we can express the RIP as

$$\begin{aligned} s_{\max} &:= \max \frac{\|Ax_s\|_2^2}{\|x_s\|_2^2} \leq (1 + \delta_s) \\ s_{\min} &:= \min \frac{\|Ax_s\|_2^2}{\|x_s\|_2^2} \geq (1 - \delta_s). \end{aligned} \quad (4)$$

Given that the vector x_s is s -sparse, s_{\min} is the square of the minimum singular value of all $m \times s$ submatrices [15] of A . It is known that in inverse-scattering problems, the singular values of A rapidly decay after a certain threshold, so the minimum singular value is close to zero [33]. As the number of nonzero entries in x increases (i.e., s increases), the minimum singular value decreases and for some s , the second condition in (4) is violated. We note in passing that in related literature on sparse targets (i.e., small values of s), RIP may hold if the s th singular value (when the singular values are arranged in decreasing order) is in a range similar to the maximum singular value.

IV. JOINT NORM FORMULATION

If we can modify the matrix A in such a manner that the minimum singular value of all submatrices can satisfy (4), the

RIP can be satisfied. One of the ways to achieve it is by using Tikhonov regularization. A Tikhonov regularized cost function is written as

$$\begin{aligned} J1(x) &= \|Ax - y\|_2^2 + \lambda_2 \|x\|_2^2 \\ J1(x) &= \|\mathcal{A}x - y\|_2^2 \end{aligned} \quad (5)$$

where we use the notation: $\mathcal{A} := [A \sqrt{\lambda_2} I]^T$ and $y := [y \ 0]^T$, and λ_2 is a regularization parameter.

The regularization boosts the minimum singular value by $\sqrt{\lambda_2}$, so for an appropriate value of λ_2 , RIP can hold for the matrix \mathcal{A} . The updated conditions of (4) for the new matrix become

$$\begin{aligned} \lambda_2 + s_{\max} &\leq (1 + \delta_s) \\ \lambda_2 + s_{\min} &\geq (1 - \delta_s). \end{aligned} \quad (6)$$

There is an upper bound [27] of $\sqrt{2} - 1$ on the value of δ_s for the exact recovery of the reconstruction problem in (2). For any $\delta_s < \sqrt{2} - 1$, if λ_2 is selected within $[1 - \delta_s - s_{\min}, 1 + \delta_s - s_{\max}]$, (6) is satisfied and thus RIP holds.

As an example, choose $s = \|x\|_0$ for the unknown vector x of the geometry in Example 1 of Section V. The average values (over many submatrices of A) of s_{\max} and s_{\min} converge to 0.55 and 2.1×10^{-6} , respectively. Clearly, the RIP is not satisfied for this s_{\min} . For the matrix \mathcal{A} , if we choose $\delta_s = \sqrt{2} - 1$, the range for λ_2 is $[0.59, 0.86]$. Picking a value of λ_2 as 0.65, we get $s_{\max}^{\mathcal{A}} = 1.20$ and $s_{\min}^{\mathcal{A}} = 0.65$, and these values satisfy the conditions in (4).

In this paper, we justify the need of the joint norm and extend our previous work [34] with additional *a priori* information by means of placing box constraints on the unknown permittivity. For example, we assume that the relative permittivity of materials of interest must be greater than that of vacuum. Real part of the contrast is a relative measure with respect to the background and the background can have a value higher than that of the object. Thus, by considering two extreme values for background, namely lowest (vacuum) and highest ($\epsilon_{b,\max}$), the range of permittivity contrasts for all materials we get is $(-1 + 1/\epsilon_{b,\max}, \epsilon_{\max} - 1]$. Similarly, the range for conductivity contrast is $[-\sigma_{\max}/\epsilon_0\omega, 0]$. Here, ϵ_{\max} and σ_{\max} represent the maximum relative permittivity and the maximum conductivity of the domain, respectively. Thus, our cost function becomes

$$J(x) = \|\mathcal{A}x - y\|_2^2 + \lambda_1 \|x\|_1, \quad x \in X \quad (7)$$

where λ_1 is a regularization parameter of the $L1$ constraint, and X is the feasible set for the unknown vector x . It should be noted that the λ_1 and λ_2 parameters are not related in any way, and are assumed to take any values in \mathbb{R}^+ . Our solution strategy is essentially to estimate one parameter by minimizing the residue, while holding the other parameter constant.

Our approach to solve the optimization problem is based on the ability to efficiently solve Lasso problems such as (7) (where a least-squares solution is sought with a constraint on the $L1$ norm of the solution) using the spectral projected gradient method [35] with range constraints and to update the λ_2

Algorithm 1. Inverse scattering algorithm

```

procedure JOINT NORM REGULARIZED ALGORITHM ( $\mathcal{A}$ ,
 $x, y, \tau, \lambda_2, \gamma, \delta, \epsilon, \delta_r, l_m$ )
  set initial  $r_0 \leftarrow \mathcal{A}x - y$ 
  set initial  $g_0 \leftarrow \mathcal{A}^H r_0$ 
  set initial  $l \leftarrow 0$ 
  set  $f_l \leftarrow \|r_0\|_2^2$ 
  define  $\hat{f}_l = \Delta f / f_l$ 
  define  $\hat{x}_l = \Delta x / x_l$ 
   $X$  is the feasible set
  while ( $f_l \geq \gamma \|l < l_m$ ) do
    if  $\hat{f}_l \leq \delta \| \hat{f}_l \leq \delta_r \|r_l\|_2$  then           % update  $\tau$ 
       $\tau \leftarrow \tau + \Delta\tau$ 
    end if
    if  $\hat{f}_l \leq \delta \ \& \ \| \hat{x}_l \|_1 \leq \epsilon$  then           % update  $\lambda_2$ 
      estimate  $\lambda_2$ 
      update  $\mathcal{A}$ 
    end if
    estimate  $\alpha$            % Barzilai – Borwein steplength
     $g_l \leftarrow \mathcal{A}^H r_l$ 
     $x_{l+1} \leftarrow \Pi_X(x_l - \alpha g_l)$            % residue min.
     $r_{l+1} \leftarrow \mathcal{A}x_{l+1} - y$ 
    set  $f_{l+1} \leftarrow \|r_{l+1}\|_2^2$ 
     $l \leftarrow l + 1$ 
  end while
end procedure

```

parameter if and when necessary. This problem when solved as a Lasso problem is similar to [36] and [37]. However, those approaches can be thought of as a special case of our generalized approach (no box constraints and $\lambda_2 = 0$).

Let us define $\|x\|_1 = \tau$. The value of τ is related to λ_1 as follows. As the value of τ increases, the value of λ_1 should be decreased to keep the contribution of the $L1$ norm term to $J(x)$ at a minimum. Thus, for appropriate choices of the parameters, solving the problem using τ or using λ_1 is equivalent. We consider the first approach (fixing $\|x\|_1 = \tau$) to solve our problem. Hence, the cost function becomes

$$J(x) = \|\mathcal{A}x - y\|_2^2 \quad \text{s.t.} \quad \|x\|_1 \leq \tau, \quad x \in X. \quad (8)$$

The overall approach we use for solving this optimization problem is outlined in Algorithm 1 and elaborated further below. The key symbols are listed in Table I. In the algorithm, $\gamma, \delta, \epsilon,$ and δ_r are error thresholds and l_m is the maximum number of iterations. The algorithm has three key steps, which are iterated until a convergence criterion is satisfied: 1) updating the $L1$ norm constraint τ ; 2) minimizing the residue using the projected gradient method by deploying the joint norm regularization; and 3) estimating the parameter λ_2 .

A. Update of the $L1$ Norm Constraint τ

Assume that at a given iteration, we have an estimate of x for a given τ , but that the residue still needs reduction, i.e., the convergence criterion has not been satisfied. In such a case, τ has to be updated, generally to a larger value. We follow the

TABLE I
KEY SYMBOLS USED IN THE PAPER

x	Vector of unknown dielectric contrasts
X	Feasible set for the unknown dielectric contrast
\mathcal{A}	New matrix generated by appending $L2$ norm based constraint to the system matrix A
y	Updated the measurement vector
λ_1	Regularization parameter for $L1$ norm based constraint
λ_2	Regularization parameter for $L2$ norm based constraint
τ	$L1$ norm of x
c	New x in the gradient direction
b	Upper or lower bound of x , decided based on the sign of c
θ	Lagrangian parameter for τ based constraint
χ_{med}	Normalized median value of the relative permittivity
S	Proportion of the number of measurements to total number of unknowns
C_o	Percentage of pixels correctly classified as background
C_i	Percentage of pixels correctly classified as the object

method described in [36], where τ is expressed as a differentiable, convex, and strictly decreasing function $\phi_1(\tau)$. The function represents an $L1$ constrained minimization problem ($\min_x \|Ax - y\|_2$ s.t. $\|x\|_1 \leq \tau$) in a dual-norm formulation [38]. Mathematically, the function is written for a variable $z \in \mathbb{C}^n$ as follows:

$$\phi_1(\tau) = \inf_x \left(\|Ax - y\|_2 + \sup_z (x^H z - \tau \|z\|_\infty) \right). \quad (9)$$

For the optimum value of $x := \tilde{x}$ at a given τ , this function (called $\tilde{\phi}_1(\tau)$) becomes $\|A\tilde{x} - y\|_2$. This monotonically decreasing function can be solved using Newton's root finding method [39]. At each iteration, we update our previously estimated τ with an increment

$$\Delta\tau = -\frac{\phi_1(\tau)}{\phi_1'(\tau)} = \frac{\tilde{\phi}_1(\tau)^2}{\|A^H(A\tilde{x} - y)\|_\infty}.$$

B. Minimize the Residue Using Projected Gradient Method

Given the parameters τ and λ_2 , the given optimization problem becomes

$$\underset{x}{\text{minimize}} \|Ax - y\|_2^2 \quad \text{s.t.} \quad \|x\|_1 \leq \tau, \quad x \in X. \quad (10)$$

We rely on a projected subgradient method to get a feasible solution [35]. Projected subgradient methods minimize a function in the variable x subject to a constraint $x \in X$, by generating a sequence x_l via

$$x_{l+1} = \Pi_X(x_l - \alpha g_l) \quad (11)$$

where g_l is the subgradient (gradient for nondifferentiable function ($L1$ projection) [40]) of the function, α is the step length and $\Pi_X(x)$ is projection of x on X . Here, the projection also encompasses the $L1$ constraint. This minimization has two steps to perform: 1) minimize the residue using the gradient method and 2) project the estimate from the previous on the feasible set. For step 1), at every iteration, the functional $\|Ax - y\|_2^2$ is minimized by moving in the opposite direction of the gradient and estimating the step length (computed using the method in [37]). For step 2), the unconstrained update $c_{l+1} := x_l - \alpha g_l$ has to be projected, which is discussed subsequently.

C. Projection on a Feasible Set

The projection has to be performed in a way that the estimated x_{l+1} satisfies the $L1$ norm constraint and is within the bounds. We want to estimate x_{l+1} from the current gradient estimate c_{l+1} by solving the following optimization problem:

$$\begin{aligned} \min_x \|c - x\|_2^2 \quad \text{s.t.} \quad & \|x\|_1 \leq \tau, \quad x_{i,\min} \leq x_i \leq x_{i,\max}, \\ & i = 1, \dots, n \end{aligned} \quad (12)$$

where the iteration number has been omitted for better readability, $x_{i,\min} \in \mathbb{C}$ and $x_{i,\max} \in \mathbb{C}$ are bound constraints on x_i , which defines the feasible set X . Both are assigned based on *a priori* information. Different constraints for each x_i can incorporate more priors than constant bounds. The priors could include, apart from obvious range restriction on x_i , positions and electric properties of the background medium. It can also include solutions of other methods.

We solve this problem by formulating in the Lagrangian form and considering the first-order Karush–Kuhn–Tucker (KKT) conditions. Each element of x , x_i is estimated using the following relations, where b_i is one of the bounds, chosen based on sign of c_i , and θ is the Lagrangian parameter corresponding to the $L1$ constraint (refer to Appendix for details)

$$x_i = \begin{cases} 0, & \text{if } |c_i| \leq \theta \\ b_i, & \text{if } |c_i| > b_i + \theta \\ |c_i| - \theta, & \text{if } \theta < |c_i| \leq b_i + \theta. \end{cases} \quad (13)$$

D. Update of the Parameter λ_2

As mentioned earlier, the value of λ_2 has to be chosen in an interval as per (6). However, this interval is not known *a priori* for all values of the sparsity parameter s and moreover, the value of s itself is unknown. So, rather than fixing s or using the same interval for all cases, we obtain the interval from the current estimate of x , and then select one value from it.

There are various methods in the literature which describe the estimation of λ_2 and also solve the Euclidean norm problem [5], [41], [42]. We use a method described in [43] because it can be easily altered to estimate λ_2 within a given interval.

Mead [43] extended Rao's fundamental theorem [44] to $L2$ regularized cost functions, stating that when model covariance matrix C is available, we may choose the data (x in our case) inverse covariance matrix C_x^{-1} such that the cost function follows a χ^2 distribution with mean m_χ , as closely as possible. If we assume $C_x^{-1} = \lambda_2 I_n$, then our cost function in (8) (without the $L1$ norm constraint) for the current estimate of x can be equivalently written as $\phi_2(\lambda_2) = (Ax - y)^H C^{-1} (Ax - y) + \lambda_2 \|x\|_2^2$. To satisfy Mead's theorem, the cost function should stay within the following range:

$$m_\chi - \sqrt{2m_\chi} z_{\alpha/2} < \phi_2(\lambda_2) < m_\chi + \sqrt{2m_\chi} z_{\alpha/2} \quad (14)$$

where $z_{\alpha/2}$ is the z -value for a standard normal distribution having $(1 - \alpha)$ confidence interval. If the tolerance related to confidence interval parameter α is low, the above

inequality approximately equals the following equation after some algebra:

$$\begin{aligned} & \phi_2(\lambda_2) \\ &= r^H \left((L^{-1})^H U \operatorname{diag} \left(\frac{1}{1 + \frac{\sigma_i^2}{\lambda_2}} \right) U^H L^{-1} \right) r - m_\chi \approx 0 \end{aligned} \quad (15)$$

where L is Cholesky factorization matrix of C , U is the matrix corresponding to the SVD of $L^{-1}A$ as $U\Sigma V^H$, and σ_i , $i = 1, \dots, m$ are the singular values of $L^{-1}A$.

The equation is monotonically increasing as λ_2 varies from 0 to ∞ . It is solved using the Newton root finding algorithm, where we search for λ_2 within the current estimate of the interval. If the root exists and is positive, it is unique [43]. There are two other possibilities: 1) $\phi_2(0) > 0$, which effectively suggests that the equation does not need any regularization and we set $\lambda_2 = 0$; and 2) $\phi_2(\infty) < 0$, which indicates that no root exists. Here, we choose not to assign any value to λ_2 and use the previously estimated value.

The advantage of this approach is that model parameters come directly from the experiment, thus avoiding any tuning parameters. It also considers statistical information available to define a physically meaningful regularization.

E. Undoing the Effect of Regularization

An $L2$ norm-based solution scales the solution and an $L1$ norm-based solution translates the solution [12]. Since the parameters are updated throughout the minimization, we consider the final values of the parameters as the scale/translation factors and use them to undo the effect. The scaling factor is not known *a priori* and is not easy to determine, so we apply the same factor which is known for the orthonormal case, i.e., $(1 + \lambda_2)$. The translating factor is θ , which is the same θ as in (13). Generally, τ is higher than $\|x\|_1$ and therefore θ is zero. Therefore, we do not apply any correcting factor for the $L1$ regularization.

V. NUMERICAL ANALYSIS AND RESULTS

We performed several experiments to validate the proposed method. In the reported numerical results, scattered field data have been obtained by using the FEM. In order to avoid inverse crime, the mesh used for solving the forward problem has been chosen finer than that used for the inverse problem.

The simulation configuration is as follows: The transmitting and receiving antennas are located at 20° apart from each other on the circumference of the circular domain of radius 1.5λ (free-space wavelength). The operating wavelength is 14.28 cm and the domain is meshed at $\lambda/100$ to maintain the error in field calculation within bound.

The object domain used for calculating scattered field is a circular domain of radius 1λ . The domain is meshed at $\lambda/17$ for the “measured” scattered field integral and at $\lambda/50$ for the forward solver. This gives an image size of 34×34 pixels inscribing the circular domain and thus the number of unknowns (only in the circular domain) for the inverse problem has

$2 * 912 = 1824$ pixels. The total number of measurements is $18 * 18 = 324$, making the inverse problem underdetermined.

When we estimate λ_2 , the model covariance matrix C is considered to be the identity matrix (because noise is zero). The bound for x is uniform for all pixels. Initially, the value for τ is set to zero. The starting point for vector x is the minimum energy solution ($A^H y$) and λ_2 is estimated using this residue. Each image is formed with seven iterations of BIM. An iteration consists of one run of the forward solver and up to 150 gradient iterations. The computation time to run a single forward solver is approximately 60 s for code written in C++ and average time to run inverse problem is approximately 80 s for code written in MATLAB on a Linux desktop with a Xeon processor and 24-GB RAM.

Example 1: Circular cylinder: Here, the object under test is a homogeneous circular cylinder located at the center. The cylinder is 0.8λ in diameter and has a relative permittivity of 2.5. The background is air. The reconstructed cylinders are shown in Fig. 1. The actual object and its real and imaginary permittivities are shown in Fig. 1(a) and (e), respectively. We compare the reconstruction performance by the joint norm to the performance by using only $L2$ norm. As discussed in Section IV-D, any method can be incorporated for λ_2 estimation. To make a fair comparison, we have used the same method as has been used in our joint norm, i.e., set $\lambda_1 = 0$, and apply positivity bound constraints for the real part of x and negativity constraints for the imaginary part of x . Fig. 1(b) and (f) shows the reconstruction of real and imaginary parts of the permittivity, respectively, using just $L2$ norm. As expected and can be seen, the objects in the images are smoothed and also the imaginary part has nonzero values. Fig. 1(c) and (g) shows the reconstruction of the permittivity using joint norm with the same constraints as using just $L2$ norm. These figures clearly show the improvement in the sparsity of the background. The energy leakage in the imaginary part can be understood by the facts that y is not in the range of \mathcal{A} in the linearized BIM approach and the system is a highly underdetermined system.

If we have *a priori* information that the domain is lossless, bound on permittivity can be set to $[1 + j0, 3.5 + j0]$. The corresponding images are shown in Fig. 1(d) and (h). The real part image has recovered higher contrast and image of the imaginary part remains as is. In all of the cases, the object is detected at the correct location and its shape has been recovered with sharp boundaries. The peak relative permittivity at last iteration is approximately 2.72. Fig. 2 shows the cross-sectional (horizontal) view of the actual and reconstructed permittivity using joint and just $L2$ norm. Only $L2$ norm-based reconstruction underestimates the contrast and has nonzero values in background. The joint norm method estimates a reasonably good contrast and also produces a background that is very close to zero.

To quantify our observations, we used the following performance metric: $C_o(C_i)$ is the ratio of the number of pixels from outside (inside) the object classified as background (object) to total number of pixels outside (inside) the object. We have used two thresholds to determine the class of each pixel: 1) lower threshold (1% in our case): all pixels below this level are classified as background; and 2) upper threshold (we took this to be 30% of the contrast): all pixels above this value are

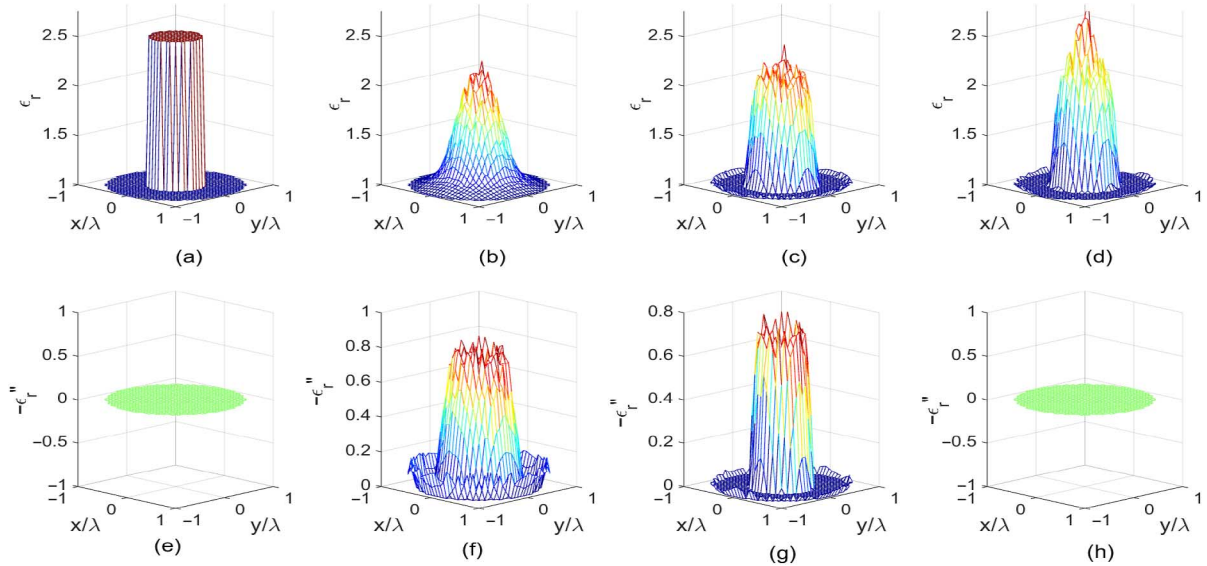


Fig. 1. Relative permittivity distribution for (a) actual object, (b) using just L_2 norm with positivity constraint, (c) using joint norm with positivity constraint, and (d) using joint norm with permittivity bound of [1, 3.5]. Imaginary part of permittivity for (e) actual object, (f) using just L_2 norm with negativity constraint, (g) using joint norm with negativity constraint, and (h) using joint norm being zero. Imaginary part is shown as $-Im$.

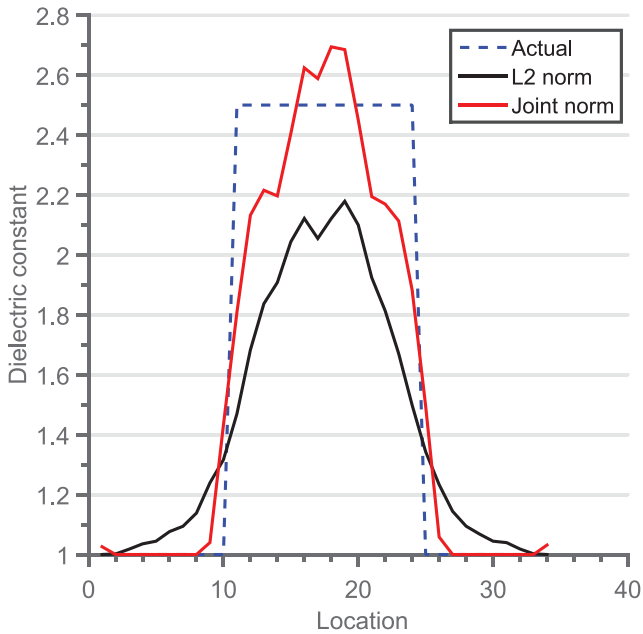


Fig. 2. Horizontal cross-sectional view from the center of the cylinder; the plot of real part of permittivity versus image points. Blue dotted line corresponds to actual profile, red line corresponds to joint norm, and black line corresponds to L_2 norm.

classified as object. The metric is applied to both permittivity images separately. Table II shows the performance values for all reconstructed objects. In the ideal case, C_o and C_i are 1. As can be seen from Table II, the reconstruction of imaginary part of permittivity using joint norm is ideal. The contrast leakage into the background for L_2 norm-based approach is captured by a very small value of C_o . The improvement in contrast estimation using joint norm is evidenced by the high value of C_i .

The effect of noise on the quality of reconstruction has also been analyzed. We added white Gaussian noise with zero mean.

TABLE II
QUANTITATIVE MEASUREMENT OF THE RECONSTRUCTED IMAGES

Object	ϵ	L2 norm				Joint norm			
		C_o real	C_i real	C_o imag.	C_i imag.	C_o real	C_i real	C_o imag.	C_i imag.
Circular	2.5	0.27	0.93	0.44	0	0.87	1	1	1
Circular	$-j1.5$	0.64	0.67	0.40	0.59	1	1	0.77	0.91
Rectangular	2.5	0.07	0.62	0.07	0	0.90	0.97	1	1
Rectangular	$1.6 - j0.8$	0.52	0.75	0.24	1	0.84	0.96	0.91	1
Triangular	2.5	0.05	0.92	0.1	0	0.87	1	1	1
Chilli	$1.6 - j0.7, 2.1 - j0.3$	0.38	0.47	0.56	0.82	0.76	0.74	0.85	0.98
Three objects	2.5, 2.1, 1.9	0.52	0.97	0.20	0	0.89	0.93	1	1
Rings in a box	2.5	0.45	0.70	0.22	0.1	0.85	0.95	1	1
Big triangular	2.5	0.01	0.5	0.32	0	0.57	0.91	1	1
High contrast 1	3	0.01	0.97	0.65	0	0.81	1	1	1
High contrast 2	3.5	0.01	0.37	0.24	0	0.71	0.50	1	1
High contrast 3	4	0.01	0	0.24	0	0.59	0.1	1	1
High contrast 4	6	0.01	0	0.24	0	1	0.03	1	1

Fig. 3 reports the errors (whole domain) for several values of SNR (defined with respect to the scattered field as in [29]). The quantity χ_{med} represents the normalized median value of the relative permittivity. Mathematically, $\chi_{med} = \frac{\text{median}(\epsilon_r^l)}{\epsilon_r^o}$, where ϵ_r^l is the estimated relative permittivity at l object points and ϵ_r^o is the average value of the original relative permittivity of the object. As can be seen, contrast recovery is almost constant after 10-dB SNR, whereas C_i reaches a maximum value of 1 for the no-noise case. C_o keeps its value around 90% for all SNR values. Overall, the contrast is very well recovered for all SNRs

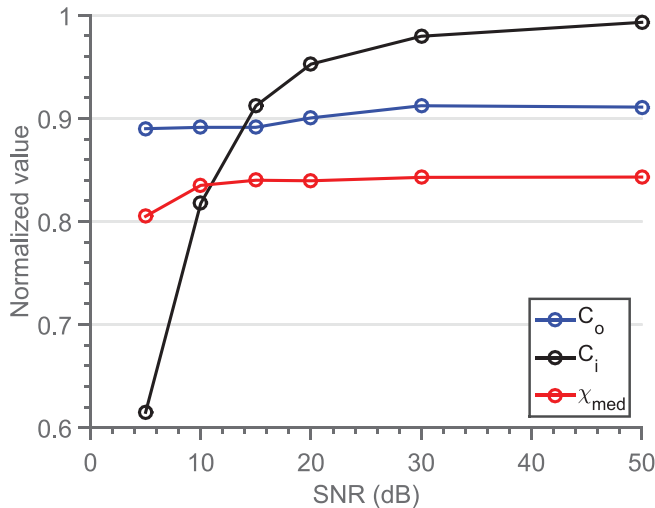


Fig. 3. Performance at various SNR values.

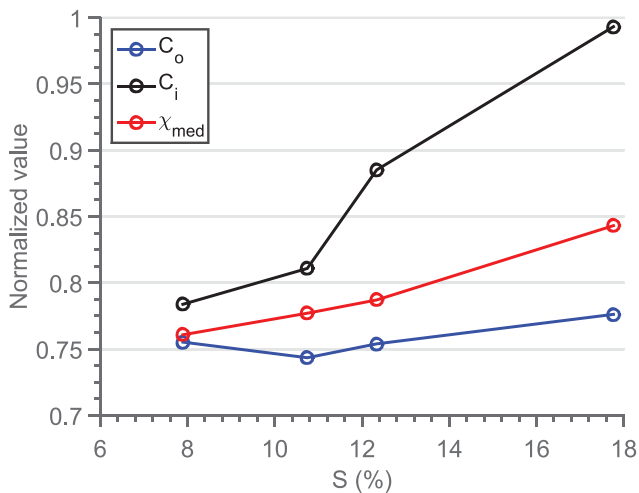


Fig. 4. Plot for performance of the reconstruction versus the ratio of the number of measurements to total number of unknowns.

and the object is also localized correctly showing that noise at these levels does not have a major impact on the performance. We have also analyzed the effect of the number of measurements on the reconstruction quality. Fig. 4 shows the plot for C_i , C_o , and χ_{med} values for various values of S . The quantity S is the proportion of the number of measurements to total number of unknowns. As the number of measurements increase, the quality of reconstruction becomes better. However, we do not always have the luxury of having a large number of measurements in practice. Still, we still have reasonable accuracy for $S = 8\%$. Next, using the same geometric parameters, we have formed an image of a cylinder having the imaginary part of permittivity -1.5 as shown in Fig. 5(a) and (d). The complex permittivity recovery is shown in Fig. 5(c) and (f). The object is detected with good estimated conductivity contrast. The reconstruction using just $L2$ norm is also shown in Fig. 5(b) and (e). We have used the same constraints for both cases: positivity for real part and negativity for imaginary part. The conductivity contrast is underestimated for just $L2$ norm. The real part is zero everywhere for joint norm, which is significantly different

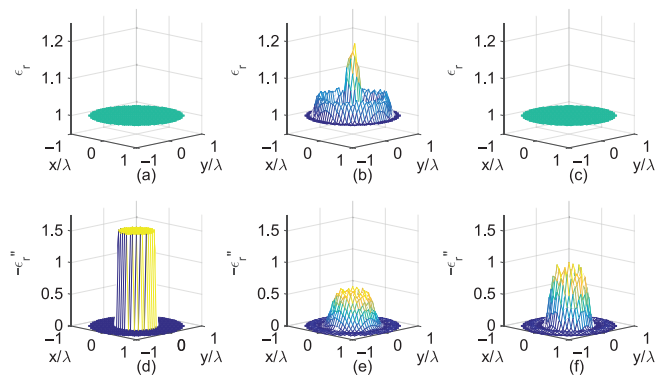
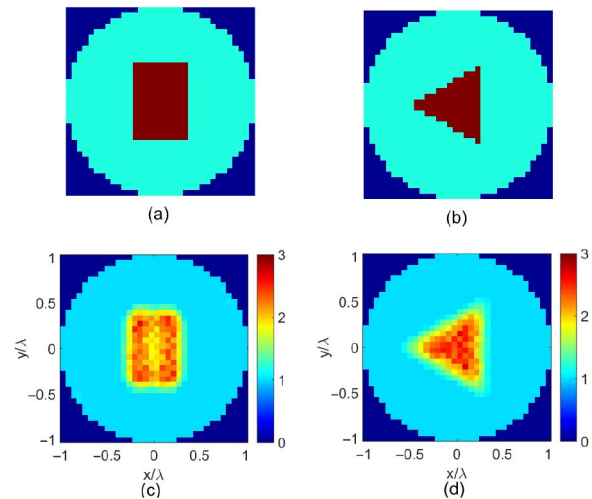

 Fig. 5. Distribution of real part of permittivity for (a) original configuration, (b) just $L2$ norm recovery, (c) joint norm recovery. Distribution of the negative of imaginary part of permittivity for (d) original configuration, (e) just $L2$ norm recovery, (f) joint norm recovery.


Fig. 6. Original geometry for (a) rectangular cylinder, (b) triangular cylinder. Distribution of relative permittivity recovered using the joint norm for (c) rectangular shape object, (d) triangular shape object. The colormap shows the relative permittivity.

from that for $L2$ norm. Minimum $L1$ norm-based constraint has played a role to make it sparse.

Example 2: Other shape cylinders: The object is a homogeneous rectangular cylinder located at the center of the domain. The rectangle is $0.5\lambda \times 0.8\lambda$ [shown in Fig. 6(a)] and has a relative permittivity of 2.5. The reconstructed distribution is shown in Fig. 6(c). As can be seen, there is a good agreement with the actual configuration. Corresponding values for C_o and C_i are reported in Table II. The bound is $[1 + j0, 3.5 + j0]$. The cross-sectional view of the recovery for joint norm and $L2$ norm is shown in Fig. 7(a). The edge of the rectangular cylinder is detected at the correct positions for joint norm, whereas $L2$ norm-based approach fails to localize the object. Next, when the object is not loss-less and has complex permittivity $(1.6 - j0.5)$, joint norm-based approach is still able to recover both parts correctly. The reconstruction quality is shown in Fig. 8 and the quantitative values are reported in Table II. Here, the bound is $[1 - j1.5, 3.5 + j0]$. Next, we have considered a cylinder having the shape of a triangle, which is also located at the center [Fig. 6(b)]. The equilateral object has a side-length of

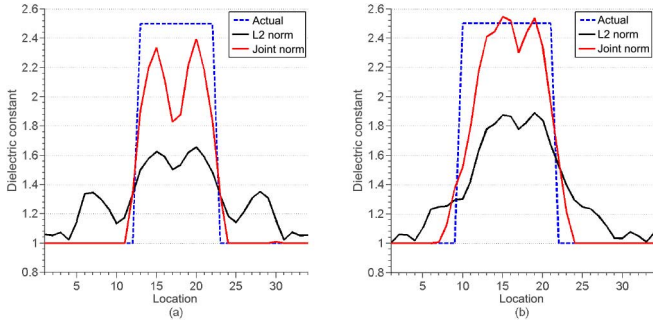


Fig. 7. Cross sectional view of relative permittivity retrieval for (a) rectangular cylinder and (b) triangular cylinder.

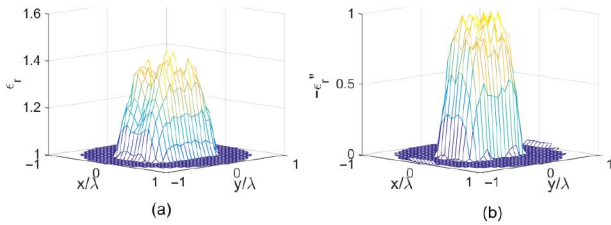


Fig. 8. Complex permittivity retrieval for rectangular cylinder. (a) real part of permittivity, (b) negative of imaginary part of permittivity.

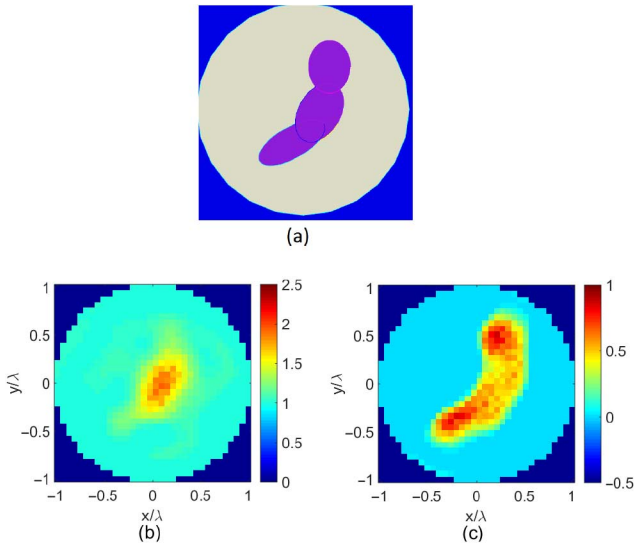


Fig. 9. (a) Actual chili-shaped object. The reconstructed distribution of (b) real part of permittivity, (c) negative of imaginary part of permittivity. The colormap shows the relative permittivity.

0.866λ and has a relative permittivity of 2.5. The reconstruction after seven BIM iterations is shown in Fig. 6(d). The triangle’s edges are well localized. The recovered peak relative permittivity is 2.62. The bound is also the same as the bound used in recovering only relative permittivity for the circular cylinder. The localized quality shown in Fig. 7(b) is also supported by having high values for performance metric (Table II).

Example 3: Chili-shaped object: In this example, the object is composed of three ellipses placed close to each other to generate an irregular “chilli”-shaped object as shown in Fig. 9(a). The complex permittivity is (1.6 − j0.7) at head and toe of the object and (2.1 − j0.3) at remaining places. Fig. 9 shows

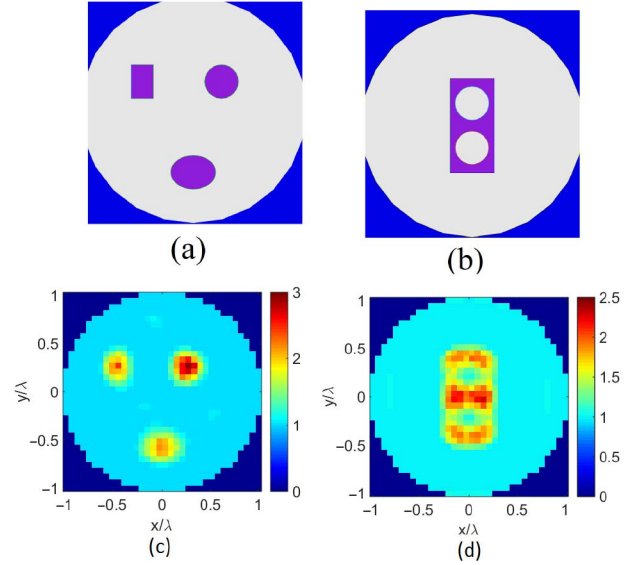


Fig. 10. (a) Original image for three objects configuration, (b) original image for two void holes in the box. Distribution of the recovered relative permittivity for (c) three objects and (d) void holes in a box. The colormap shows the relative permittivity.

reconstructed permittivity distribution. The peak values are 1.9 and −0.6, respectively, for real and imaginary parts. The bound for permittivity is [1 − j1, 3.5 + j0].

Example 4: Three objects: A more complicated object is considered here, consisting of three objects: circular, elliptical, and rectangular. Their sizes are 0.3λ in diameter, 0.4λ × 0.3λ axial length, and 0.2λ × 0.3λ side length, respectively. Their relative permittivities are 2.5, 1.9, and 2.1, respectively. The reconstruction distribution is shown in Fig. 10(c). As can be seen from Fig. 10(a), there is good agreement with the actual configuration.

Example 5: Two rings in the box: The box is characterized by relative permittivity = 2.5, length = 0.85λ, and width = 0.4λ. The circular void holes (background permittivity) of radius 0.15λ and centers at (0, −0.2λ) and (0, 0.2λ), respectively, are present inside the box cylinder. The reconstructed distribution is shown in Fig. 10(d). Comparing it with Fig. 10(b), the proposed approach provides quite good results. In particular, the algorithm is able to detect the edges of box correctly and also the location and size of the circles.

Example 6: Limits: We use sparsity-based constraints, so that if we do not apply any compressible transformations to convert nonsparse objects into sparse objects, the recovery may not be accurate. The recovery of the nonsparse object depends on the number of measurements and the size of the object. The higher the number of measurements, the larger the size of the object that can be recovered. As an example, we tried to recover the triangular cylinder of 1.4λ side length (instead of 0.866λ) and kept the same number of the measurements (324) and unknowns (1824). The permittivity was set to 2.5. The recovered object is shown in Fig. 11(a). The algorithm was not able to recover the shape but contrast has recovered reasonably well. Since the object is big, the valid range for λ₂ in some iterations is not feasible so the recovery is as good

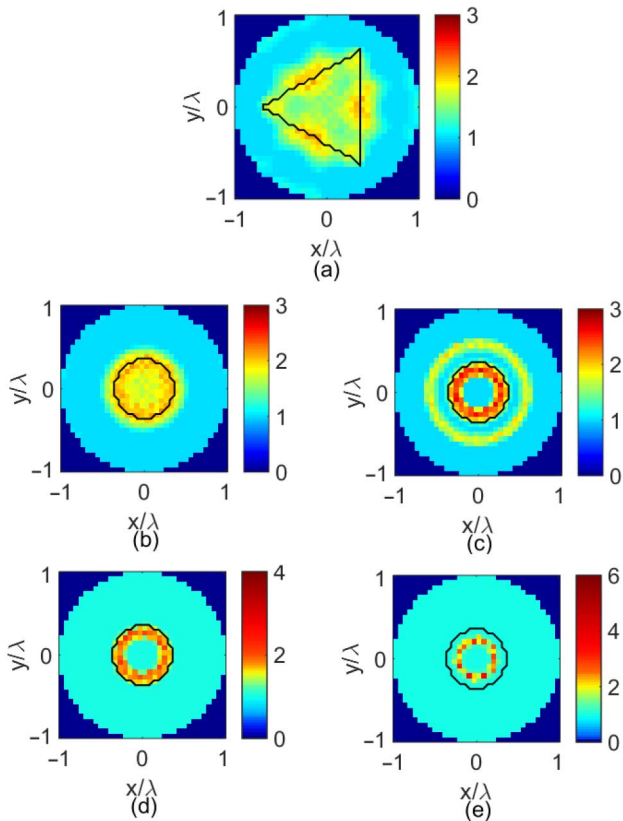


Fig. 11. (a) Large object, (b) permittivity 3, (c) permittivity 3.5, (d) permittivity 4, and (e) permittivity 6. The boundary of the actual object is overlaid (black line). The colormap shows the relative permittivity.

as just using $L2$ norm (see Table II). There are two possible ways to address the problem: 1) increasing the number of measurements and reconstruction domain so that it becomes similar to previous examples; or 2) applying a transformation (wavelet, Fourier, TV, etc.) and solving the problem in that domain (in this case, the elements of the unknown vector x become the coefficients in the transformed domain). However, the bounds cannot be known in the transformed domain and need further study. We attempted to recover a circular cylinder having a very high contrast (maximum permittivity = 6). The reconstruction results for permittivity values 3, 3.5, 4, and 6 are shown in Fig. 11(b)–(e). It is a well-known fact that the BIM-based linearized approach cannot recover very high contrasts and multiple scattering effects cannot be well incorporated in the first-order approximation. Generally, the observed limit on acceptable recovery of absolute value of permittivity is around 2.5. In our case also, the reconstruction algorithm fails to recover the shape and contrast of the object, when the contrast is higher in similar range. We can adopt DBIM or some other technique here but we are more interested to see if the sparsity constraint can recover higher contrast than other regularized methods.

Example 7: Comparative assessment. To make a fair comparison with a state-of-art TV-based compressive sensing method for inverse-scattering problem, we selected one of their results as a reference. The method is valid only in the BA region [29] so we restricted our method to run only for one iteration. We keep

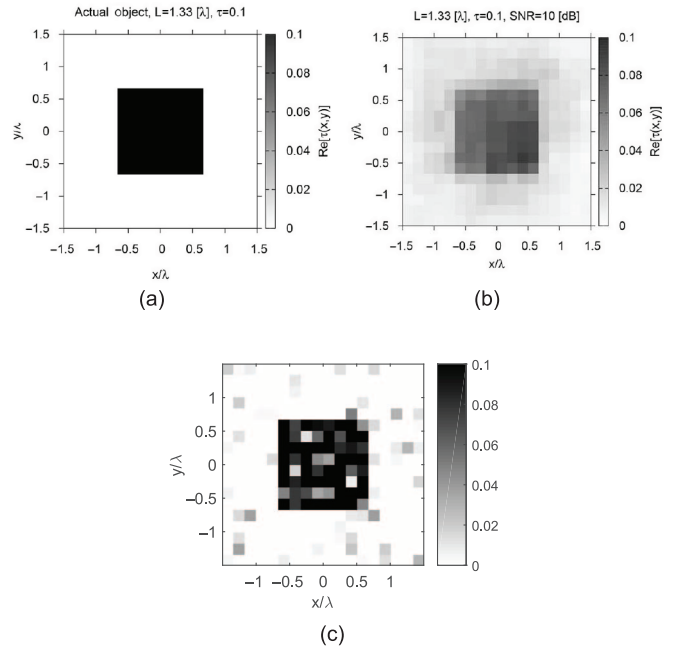


Fig. 12. (a) Square dielectric object at center; the image reprinted from Fig. 6(d) of [29] (true values), (b) reconstruction results using TV; the image reprinted from Fig. 6(g) of [29], and (c) recovery using the joint norm. The colormap shows the permittivity contrast.

the number of measurements, the geometry, and SNR same, but the synthetic data are generated using FEM with the triangular mesh. Each side of the pixel in the reconstruction domain has the length same, $\lambda/6$, as used in the TV-based method. The images of [29], reprinted in Fig. 12(a) and (b), are the original image and the image recovered using the TV-based constraint. The image reconstructed using our method is shown in Fig. 12(c). As can be seen, the joint norm-based method has more accurate and sparse reconstruction. Quantitatively, the error index ξ_{tot} , metric used in [29] to quantify the error, drops from 1.5% to 0.7%. The size of the object considered in this experiment is bigger than other experiments mentioned in the article. The reason for achieving better result for the large object is the use of larger number of measurements. We also tested the performance of the joint norm method for other examples in [29], but in the interest of space, we are not putting all the graphs but just mentioning that the joint norm method performs better than the TV-based method. It recovers the contrast much better, keeps the most of the background to zero, and also has the better definition of edges.

VI. CONCLUSION

We presented a joint $L1-L2$ norm-based regularization for inverse scattering. The proposed approach is based on sparsity and smoothness, which allows obtaining the solutions without oversmoothing at discontinuities. The joint norm can preserve the sufficient condition for the sparse recovery, if the parameters are chosen appropriately. The algorithm can also incorporate a priori information about the upper and lower bounds of the range of contrasts. The reconstructed images for various shapes showed very good shape recovery, localization,

and contrast estimation up to a contrast of about 2.5. Some theoretical open issues still exist and need further consideration. In particular, bound constraints for large objects need to be investigated, if the objects are represented in a sparsifying domain. Furthermore, recovery for higher contrasts must be analyzed. Future work includes evaluating the performance of the method on experimental data.

APPENDIX

Before starting to solve (12), let us consider the optimization problem without box constraints and also make all vectors real

$$\underset{x}{\text{minimize}} \|c - x\|_2^2 \quad \text{s.t.} \quad \|x\|_1 \leq \tau. \quad (16)$$

We note that if $\|c\|_1 \leq \tau$, then the optimization problem is trivial and the solution is $x = c$. Therefore, from now on, we assume that $\|c\|_1 \geq \tau$, which means that the optimal solution is on the boundary of the $L1$ ball, i.e., $\|x\|_1 = \tau$. Lemma 3 from Duchi *et al.* [45] states that each element of the optimal solution \tilde{x} shares the same sign as each element of the given vector c . In other words, \tilde{x} and c are in the same orthant (quadrant for 2-D). Therefore, solving the absolute value problem is equivalent to solving a sign value problem. Equation (16) can be expressed as

$$\underset{x}{\text{minimize}} \| |c| - x \|_2^2 \quad \text{s.t.} \quad \|x\|_1 \leq \tau, \quad x_i \geq 0 \quad (17)$$

and solution of (16) is $\tilde{x} = \text{sgn}(c)^T x$.

Our optimization problem is an extension of the above and it has been shown that Lemma 3 of [45] can also be applicable for a real vector's projection on a constrained box [46], provided that necessary geometric transformation has been applied. If both bounds are in the same orthant, we can apply the geometric transformation such that the bound close to zero is shifted to the origin. We also update τ by $\tau - |x_{\min}|_1$ if bounds are positive or by $\tau - |x_{\max}|_1$, if they are negative. When both bounds are in the different orthant, we select the upper bound based on the sign of c_i so that \tilde{x}_i is close to c_i . The upper bound is $-x_{i,\min}$, if $c_i < 0$ or it is $x_{i,\max}$, if $c_i > 0$. For all cases, the lower bound is always zero. Let us call the upper bound as b_i ; the equivalent problem then becomes

$$\underset{x}{\text{minimize}} \| |c| - x \|_2^2 \quad \text{s.t.} \quad \|x\|_1 \leq \tau, \quad 0 \leq x_i \leq b_i, \\ i = 1, \dots, n. \quad (18)$$

The vector x is estimated by expressing the above optimization problem in Lagrangian form

$$L(x, \theta, \zeta, \eta) = \frac{1}{2} \| |c| - x \|_2^2 + \theta \left(\sum_{i=1}^n x_i - \tau \right) \\ - \zeta^T x + \eta^T (x - b) \quad (19)$$

where $\theta \in \mathbb{R}^+$ and $\zeta, \eta \in \mathbb{R}_+^n$ are Lagrangian parameters. Differentiating with respect to x_i and comparing it with zero gives optimality condition

$$\frac{\partial L}{\partial x_i} = -|c_i| + x_i + \theta - \zeta_i + \eta_i = 0. \quad (20)$$

The complementary slackness conditions for parameters [38] are

$$\zeta_i x_i = 0, \quad \eta_i (x_i - b_i) = 0. \quad (21)$$

To satisfy all of the conditions, we get the following relations.

- 1) When $0 < x_i < b_i$, $\zeta_i = 0$ and $\eta_i = 0$. This gives $-|c_i| + x_i + \theta = 0$. $\therefore x_i = |c_i| - \theta$.
- 2) When $x_i = 0$, $\eta_i = 0$. This gives $-|c_i| + \theta - \zeta_i = 0$. Since $\zeta_i \geq 0$ we get $|c_i| \leq \theta$.
- 3) When $x_i = b_i$, $\zeta_i = 0$. This gives $-|c_i| + b_i + \theta + \eta_i = 0$. Since $\eta_i \geq 0$ we get $|c_i| \geq b_i + \theta$.
- 4) If $|c_i| > b_i$ and $\eta_i > 0$, the distance between $|c_i|$ and x_i is minimum when $x_i = b_i$. This is only true if $\eta_i > 0$ because in general $|c_i| > b_i$ can be projected inside box also.

Summarizing the relations in known variables gives the unknown x_i as in (13).

The only unknown θ is estimated similar to an unbounded problem and is detailed in [45]. The above solution for box constraints is derived assuming that $\|c\|_1 \geq \tau$. When $\|c\|_1 \leq \tau$, we still have to ensure that x is within bounds, unlike the unbounded case. The solution, when $\|c\|_1 \leq \tau$ and box constraints are active, is exactly the same as (13) except that now $\theta = 0$.

For inverse scattering, the system of equations are complex valued. The concept used for the real vector, which stated that the distance between the original and projected vectors is the lowest, if they are in the same orthant, can extend to the complex domain. Complex numbers have a phase instead of a simple sign. We define sign function for a complex number z as $\text{sgn}(z) = \frac{z}{\|z\|}$, $\forall z \in \mathbb{C}$ (we consider positive sign for $z = 0$). When we apply the sign function to a complex number, the function projects the vector on the unit circle of a complex domain (phase of a vector). Therefore, we can use the same projection method as we have applied to the real vector to a complex vector. Though the method can work very well for this polar representation of complex-valued vectors, we can alternatively use the Cartesian (real and imaginary) representation of the same vectors. We get additional sparsity if any of the two (real or imaginary) components is zero. It should be noted that the entire problem can be solved in the complex domain, while still performing projections using real and imaginary expansion of the complex vector ($c \in \mathbb{C}^n$).

REFERENCES

- [1] D. Colton and R. Kress, *Inverse Acoustic and Electromagnetic Scattering Theory*. New York, NY, USA: Springer, 2012, vol. 93.
- [2] Y. Wang and W. Chew, "An iterative solution of the two-dimensional electromagnetic inverse scattering problem," *Int. J. Imag. Syst. Technol.*, vol. 1, no. 1, pp. 100–108, 1989.
- [3] W. Chew and Y. Wang, "Reconstruction of two-dimensional permittivity distribution using the distorted born iterative method," *IEEE Trans. Med. Imag.*, vol. 9, no. 2, pp. 218–225, Jun. 1990.
- [4] P. Rocca, M. Benedetti, M. Donelli, D. Franceschini, and A. Massa, "Evolutionary optimization as applied to inverse scattering problems," *Inverse Probl.*, vol. 25, no. 12, p. 123003, 2009.
- [5] A. Tarantola, *Inverse Problem Theory and Methods for Model Parameter Estimation*. Philadelphia, PA, USA: SIAM, 2005.
- [6] S. Sibi, "Regularization and inverse problems," in *Maximum Entropy and Bayesian Methods*. New York, NY, USA: Springer, 1989, pp. 389–396.

- [7] H. W. Engl, M. Hanke, and A. Neubauer, *Regularization of Inverse Problems*. New York, NY, USA: Springer, 1996, vol. 375.
- [8] L. Tenorio, “Statistical regularization of inverse problems,” *SIAM Rev.*, vol. 43, no. 2, pp. 347–366, 2001.
- [9] R. A. Renaut, I. Hnětynková, and J. Mead, “Regularization parameter estimation for large-scale Tikhonov regularization using a priori information,” *Comput. Statist. Data Anal.*, vol. 54, no. 12, pp. 3430–3445, 2010.
- [10] L. Reichel and H. Sadok, “A new l -curve for ill-posed problems,” *J. Comput. Appl. Math.*, vol. 219, no. 2, pp. 493–508, 2008.
- [11] C. Estatico, M. Pastorino, and A. Randazzo, “A novel microwave imaging approach based on regularization in Banach spaces,” *IEEE Trans. Antennas Propag.*, vol. 60, no. 7, pp. 3373–3381, Jul. 2012.
- [12] R. Tibshirani, “Regression shrinkage and selection via the LASSO,” *J. Roy. Stat. Soc., B*, vol. 58, no. 1, pp. 267–288, 1996.
- [13] E. Candes *et al.*, *Compressive Sensing Resources*, May 2015 [Online]. Available: <http://www.dsp.rice.edu/cs>
- [14] R. G. Baraniuk, “Compressive sensing,” *IEEE Signal Process. Mag.*, vol. 24, no. 4, pp. 118–121, Jul. 2007.
- [15] D. L. Donoho, “Compressed sensing,” *IEEE Trans. Inf. Theory*, vol. 52, no. 4, pp. 1289–1306, Apr. 2006.
- [16] L. Ségui, “Sur un problème inverse en diffraction d’ondes-identification des permittivités complexes d’un matériau à partir de données en champ proche,” 2000.
- [17] E. A. Marengo, “Compressive sensing and signal subspace methods for inverse scattering including multiple scattering,” in *Proc. IEEE Int. Workshop Comput. Adv. Multi-Sensor Adapt. Process.*, 2008, pp. 7–11.
- [18] E. Marengo, R. Hernandez, Y. Citron, F. Gruber, M. Zambrano, and H. Lev-Ari, “Compressive sensing for inverse scattering,” in *Proc. 25th URSI Gen. Assem.*, Chicago, IL, USA, 2008 [Online]. Available: <http://citeseerx.ist.psu.edu/viewdoc/download?doi=10.1.1.122.1913&rep=rep1&type=pdf>
- [19] G. Oliveri, P. Rocca, and A. Massa, “A Bayesian-compressive-sampling-based inversion for imaging sparse scatterers,” *IEEE Trans. Geosci. Remote Sens.*, vol. 49, no. 10, pp. 3993–4006, Oct. 2011.
- [20] L. Pan, X. Chen, and S. P. Yeo, “A compressive-sensing-based phaseless imaging method for point-like dielectric objects,” *IEEE Trans. Antennas Propag.*, vol. 60, no. 11, pp. 5472–5475, Nov. 2012.
- [21] L. Poli, G. Oliveri, and A. Massa, “Microwave imaging within the first-order born approximation by means of the contrast-field Bayesian compressive sensing,” *IEEE Trans. Antennas Propag.*, vol. 60, no. 6, pp. 2865–2879, Jun. 2012.
- [22] L. Poli, G. Oliveri, P. Rocca, and A. Massa, “Bayesian compressive sensing approaches for the reconstruction of two-dimensional sparse scatterers under TE illuminations,” *IEEE Trans. Geosci. Remote Sens.*, vol. 51, no. 5, pp. 2920–2936, May 2013.
- [23] L. Poli, G. Oliveri, F. Viani, and A. Massa, “MT-BCS-based microwave imaging approach through minimum-norm current expansion,” *IEEE Trans. Antennas Propag.*, vol. 61, no. 9, pp. 4722–4732, Sep. 2013.
- [24] F. Viani, L. Poli, G. Oliveri, F. Robol, and A. Massa, “Sparse scatterers imaging through approximated multitask compressive sensing strategies,” *Microw. Opt. Technol. Lett.*, vol. 55, no. 7, pp. 1553–1558, 2013.
- [25] L. Poli, G. Oliveri, and A. Massa, “Imaging sparse metallic cylinders through a local shape function Bayesian compressive sensing approach,” *J. Opt. Soc. Amer.*, vol. 30, no. 6, pp. 1261–1272, 2013.
- [26] L. Guo and A. Abbosh, “Microwave imaging of non-sparse domains using born iterative method with wavelet transform and block sparse Bayesian learning,” *IEEE Trans. Antennas Propag.*, vol. 63, no. 11, pp. 4877–4888, Nov. 2015.
- [27] E. J. Candès and M. B. Wakin, “An introduction to compressive sampling,” *IEEE Signal Process. Mag.*, vol. 25, no. 2, pp. 21–30, Mar. 2008.
- [28] G. Oliveri, P. Rocca, and A. Massa, “Reliable diagnosis of large linear arrays—A Bayesian compressive sensing approach,” *IEEE Trans. Antennas Propag.*, vol. 60, no. 10, pp. 4627–4636, Oct. 2012.
- [29] G. Oliveri, N. Anselmi, and A. Massa, “Compressive sensing imaging of non-sparse 2D scatterers by a total-variation approach within the born approximation,” *IEEE Trans. Antennas Propag.*, vol. 62, no. 10, pp. 5157–5170, Oct. 2014.
- [30] C. A. Balanis, *Advanced Engineering Electromagnetics*. Hoboken, NJ, USA: Wiley, 1989, vol. 20.
- [31] Y. Wang and W. Chew, “An iterative solution of the two-dimensional electromagnetic inverse scattering problem,” *Int. J. Imag. Syst. Technol.*, vol. 1, no. 1, pp. 100–108, 1989.
- [32] U. Khankhoje, J. van Zyl, and T. Cwik, “Computation of radar scattering from heterogeneous rough soil using the finite-element method,” *IEEE Trans. Geosci. Remote Sens.*, vol. 51, no. 6, pp. 3461–3469, Jun. 2013.
- [33] O. Bucci and T. Isernia, “Electromagnetic inverse scattering: Retrievable information and measurement strategies,” *Radio Sci.*, vol. 32, no. 6, pp. 2123–2137, 1997.
- [34] P. Shah, U. Khankhoje, and M. Moghaddam, “Joint L_1 - L_2 regularization for inverse scattering,” in *Proc. Antennas Propag. Soc. Int. Symp. (APSURSI)*, 2014, pp. 868–869.
- [35] D. P. Bertsekas, *Nonlinear Programming*. Belmont, MA, USA: Athena Scientific, 1999.
- [36] E. Van Den Berg and M. P. Friedlander, “Probing the Pareto frontier for basis pursuit solutions,” *SIAM J. Sci. Comput.*, vol. 31, no. 2, pp. 890–912, 2008.
- [37] E. G. Birgin, J. M. Martínez, and M. Raydan, “Nonmonotone spectral projected gradient methods on convex sets,” *SIAM J. Optim.*, vol. 10, no. 4, pp. 1196–1211, 2000.
- [38] S. Boyd and L. Vandenberghe, *Convex Optimization*. Cambridge, U.K.: Cambridge Univ. Press, 2009.
- [39] W. H. Press, *Numerical Recipes 3rd Edition: The Art of Scientific Computing*. Cambridge, U.K.: Cambridge Univ. Press, 2007.
- [40] A. P. Ruszczyński, *Nonlinear Optimization*. Princeton, NJ, USA: Princeton Univ. Press, 2006, vol. 13.
- [41] P. C. Hansen, “Regularization, GSVD and truncated GSVD,” *BIT Numer. Math.*, vol. 29, no. 3, pp. 491–504, 1989.
- [42] J. Chung, J. G. Nagy, and D. P. O’Leary, “A weighted GCV method for Lanczos hybrid regularization,” *Electron. Trans. Numer. Anal.*, vol. 28, pp. 149–167, 2008.
- [43] J. L. Mead and R. A. Renaut, “A Newton root-finding algorithm for estimating the regularization parameter for solving ill-conditioned least squares problems,” *Inverse Probl.*, vol. 25, no. 2, p. 025002, 2009.
- [44] C. R. Rao, *Linear Statistical Inference and Its Applications*. Hoboken, NJ, USA: Wiley, 2009, vol. 22.
- [45] J. Duchi, S. Shalev-Shwartz, Y. Singer, and T. Chandra, “Efficient projections onto the l_1 -ball for learning in high dimensions,” in *Proc. 25th Int. Conf. Mach. Learn.*, 2008, pp. 272–279.
- [46] M. D. Gupta, S. Kumar, and J. Xiao, “ L_1 projections with box constraints,” arXiv preprint arXiv:1010.0141, 2010.



Pratik Shah (S’14) received the B.Tech. degree in electronics and communication engineering from Nirma University, Ahmedabad, India, in 2007, and the M.Tech. degree in medical imaging and image analysis from the Indian Institute of Technology, Kharagpur, India, in 2009. He is currently pursuing the Graduate degree in electrical engineering from the University of Southern California, Los Angeles, CA, USA.

From 2009 to 2012, he was a Scientist with GE Global Research, Bangalore, India. His research interests include inverse problems, inverse scattering for electromagnetic imaging, optimization methods, compressive sensing, and medical imaging and image analysis.



Uday K. Khankhoje (M’14) received the B.Tech. degree from the Indian Institute of Technology Bombay, Mumbai, India, in 2005, and the M.S. and Ph.D. degrees from the California Institute of Technology, Pasadena, CA, USA, in 2010, all in electrical engineering.

He is an Assistant Professor of Electrical Engineering with the Indian Institute of Technology Delhi, New Delhi, India. He was a Caltech Postdoctoral Scholar with the Jet Propulsion Laboratory (NASA/Caltech), Pasadena, CA, USA, from 2011 to 2012, and a Postdoctoral Research Associate with the Department of Electrical Engineering, University of Southern California, Los Angeles, CA, USA, from 2012 to 2013. His research interests include computational electromagnetics and its applications to remote sensing and inverse imaging.



Mahta Moghaddam (S'86–M'87–SM'02–F'08) received the B.S. degree (with highest distinction) from the University of Kansas, Lawrence, KS, USA, in 1986, and the M.S. and Ph.D. degrees from the University of Illinois at Urbana-Champaign, Champaign, IL, USA, in 1989 and 1991, respectively, all in electrical and computer engineering.

She is a Professor of Electrical Engineering with the University of Southern California, Los Angeles, CA, USA. Prior to that, she was with the University of Michigan, Ann Arbor, MI, USA (2003–2011) and NASA Jet Propulsion Laboratory, Pasadena, CA, USA (JPL, 1991–2003). She has introduced new approaches for quantitative interpretation of multichannel radar imagery based on analytical inverse scattering techniques applied to complex and random media. She was a Systems Engineer for the Cassini Radar and served as Science Chair of the JPL Team X (Advanced Mission Studies Team). She is a Member of the Soil Moisture Active and Passive (SMAP) Mission Science Team, and the Principal Investigator of the AirMOSS NASA Earth Ventures 1 Mission. Her research interests include the development of new radar instrument and measurement technologies for subsurface and subcanopy characterization, development of forward and inverse scattering techniques for layered random media especially for soil moisture applications, and transforming concepts of radar remote sensing to near-field and medical imaging.

Dr. Moghaddam is the Editor-in-Chief of the *IEEE Antennas and Propagation Magazine*.